

Noninvasive Internal Body Temperature Tracking With Near-Field Microwave Radiometry

Parisa Momenroodaki, *Graduate Student Member, IEEE*, William Haines^{1D}, *Graduate Student Member, IEEE*, Michael Fromandi, *Student Member, IEEE*, and Zoya Popovic, *Fellow, IEEE*

Abstract—This paper presents a study of near-field radiometry for internal temperature measurements of the human body. The radiometer has a Dicke architecture and operates in the 1.4-GHz quiet band for centimeter penetration into tissues with minimized radio frequency interference (RFI). The total blackbody power from a tissue stack is received by a probe placed on the skin, designed to receive a high percentage of the total power from a buried tissue layer. Temperature retrieval for subsurface tissue layers is performed using near-field weighting functions obtained from full-wave simulations. The calibrated radiometer is demonstrated to track the temperature of a phantom muscle tissue layer under phantom fat and skin layers within a fraction of a degree. It is shown that RFI can be reduced through the use of a second probe and adaptive processing. Measurements on the human cheek show good agreement with independent thermocouple measurements inside the mouth.

Index Terms—Blackbody radiation, microwave thermometry, near field, radio frequency interference (RFI) mitigation.

I. INTRODUCTION

TRACKING the difference between internal body temperature and skin temperature is important for a variety of medical diagnostic and treatment procedures. The internal temperature of the human body can be considerably different from that of the skin [1]. The difference between core body temperature (e.g., heart) and skin varies up to ± 2 °C [2] over the circadian cycle for a healthy person. A disrupted circadian rhythm can result in seasonal affective disorder [3], type-2 diabetes [4], and heart disease [5]. Athletes, soldiers, firefighters, and astronauts under heavy training or challenging ambient conditions can have abnormal core temperatures, resulting in hypothermia, hyperthermia, and heatstroke [6], making internal body temperature monitoring important. Heatstroke in football players can result in death if not treated promptly [7]. Internal tissue temperature is relevant in cancer detection [8], monitoring drug delivery for cancer treatment [9],

hyperthermia temperature control [10], [11], and hypothermic neural rescue of infants suffering from hypoxia-ischemia [12].

Internal temperature measurements include internal thermometers, which are generally invasive, and external ones which are nonportable, expensive, and potentially influenced by environmental conditions. Internal thermometers, such as oral, rectal, and esophageal are not convenient for long-term monitoring, are difficult to insert and can cause irritation [13]. Ingestible telemetric pills measure temperature while in the digestive track for a limited period of time [14], but are not reusable, their precise position in the body is unknown, and it has been shown that drinking cool fluids increases the error to more than 6 °C [15].

External temperature measurements include magnetic resonance imaging (MRI) and zero heat flux (ZHF). MRI grants high spatial temperature resolution, but is expensive and not portable [16]. Other active external thermometers, such as computer tomography imaging and ultrasound, stimulate the body with an applicator, while ionizing X-rays can induce cancer [17]. ZHF eliminates heat loss to the environment and makes the subcutaneous temperature equal to skin temperature where it can be measured noninvasively [1], but is not wearable and becomes less accurate for thick tissue layers that are poor thermal conductors, such as fat.

The goal of microwave thermometry is a noninvasive, fast, wearable, inexpensive, and passive device which operates at a sufficiently low frequency for several centimeters penetration into the tissues. An illustration of the approach is shown in Fig. 1. The muscle and skin temperature of a human under exercise can differ by several degrees [19], and it is important to monitor the internal temperature, e.g., in the case of heart overheating. An antenna probe in direct contact with the skin receives power from the tissue stack and is followed by a sensitive receiver, in our case a Dicke radiometer. An algorithm is then required to retrieve the temperature of specific tissue layers.

Previous work in this field includes an approach with two waveguide probes with a water bolus and a multiband radiometer at 1–4 GHz is used to retrieve temperature profile in a cooled head model [11], [12], [20]. The potential of multifrequency microwave radiometry for detecting the location of a hot spot (tumor) inside a cylindrical muscle phantom has been investigated in [21]. A company in Russia developed a radiometer instrument for breast cancer detection suitable for use in hospitals [22]. Karanasiou *et al.* [23] presented a cavity for detecting the temperature profile of

Manuscript received July 1, 2017; revised October 6, 2017; accepted November 9, 2017. Date of publication December 12, 2017; date of current version May 4, 2018. This work was supported in part by the National Science Foundation (NSF) under Grant ECCS 1202193 and in part by Gaugewear, Inc., Boulder, CO, USA. This paper is an expanded version from the IEEE MTT-S International Microwave Symposium Conference, Honolulu, HI, USA, June 4–9, 2017. (*Corresponding author: William Haines.*)

The authors are with the Department of Electrical, Computer and Energy Engineering, University of Colorado, Boulder, CO 80309 USA (e-mail: parisa.momenroodaki@colorado.edu; william.haines@colorado.edu; zoya@colorado.edu).

Color versions of one or more of the figures in this paper are available online at <http://ieeexplore.ieee.org>.

Digital Object Identifier 10.1109/TMTT.2017.2776952

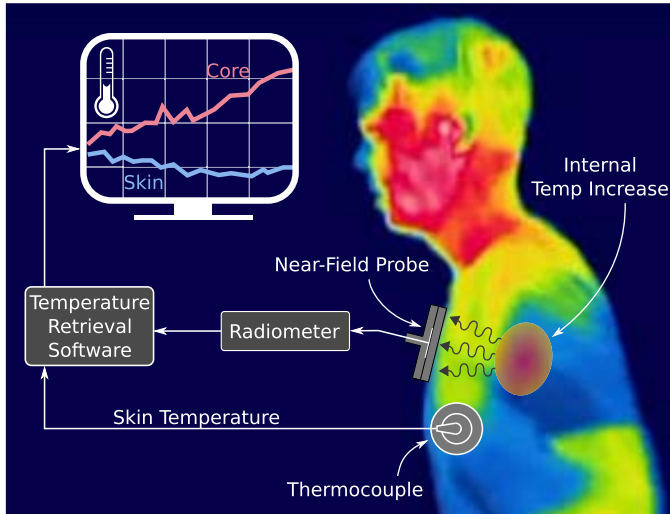


Fig. 1. Illustration of internal body thermometry using a portable microwave radiometer. A near-field probe is designed to be placed directly on the skin and couples the total received blackbody power to a calibrated sensitive receiver, followed by temperature retrieval processing. The infrared image [18] shows the temperature of the skin, which follows a different trend than muscle temperatures during exercise [19].

a simplified human head model. A near-field patch antenna array for the radiometric sensing of food temperature is described in [24]. A combination of microwave heating and radiometry as a means of the noninvasive measurement of blood perfusion is investigated in [25]–[27]. A noncontact cavity-backed slot probe was developed to work at 1.4 GHz on a tissue phantom stack of high-permittivity models for skin, muscle, and blood [28]. Different radiometer and probe designs have been investigated to work on human head and kidney phantoms [29], [30]. The efficiency of a log-spiral probe was investigated on the human head phantom in [31].

The goal of the work presented in this paper is the demonstration of a wearable device for a variety of internal body temperature measurements. Challenges include understanding blackbody radiation in the near field, efficient probe design that includes tissue properties and variation of tissue layers across the body, compact sensitive stable radiometer design, estimating internal temperature from total power external measurements, and radio frequency interference (RFI) mitigation. Initial results with a nonoptimized probe and radiometer are presented in [31] and [32], and the work here extends the results to a calibrated sensor with subdegree resolution with an improved probe design and validation of temperature retrieval algorithms for single-, two-, and three-layer tissue phantoms using a new measurement method. In addition, a two-probe radiometer for RFI mitigation is introduced and shows improved performance, and a study of the effect of tissue thickness variation is presented.

Section II discusses reciprocity between absorption and emission in the near field, showing that simulating volume power loss density in the body due to a transmitting probe on the skin can predict the emitted power from the volume received by the same probe. A circular miniaturized patch probe with a superstrate is presented and shown to have good properties on the cheek stack, as described in Section III, along

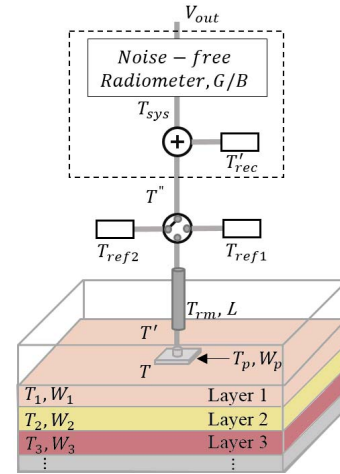


Fig. 2. Illustration of microwave radiometry for internal temperature measurements using a skin-mounted probe. The probe is at a physical temperature T_p and is on top of a tissue layer stack with temperatures T_i . The Dicke radiometer measures the total radiated power from the stack, and the weighting functions of each layer (W_i) are used to retrieve layer temperatures.

with a simple Dicke radiometer implemented with off-the-shelf components. Section IV presents tissue temperature retrieval using weighting functions for each tissue layer. Measurements on single-, two-, and three-layer phantoms are presented in Section V and compared to thermocouple measurements. Section VI discusses errors due to RFI and presents a signal processing method that can mitigate this interference. In the final section, a measurement on a human cheek is compared to internal and external thermocouple data showing that thermal conduction does not dominate the measurements, since receiving blackbody radiation is practically instantaneous.

II. MICROWAVE THERMOMETRY PHENOMENOLOGY

All objects at nonzero absolute temperature radiate power across the entire electromagnetic spectrum according to the blackbody radiation law [34], which can be approximated by white noise in the microwave region, with a total power in a bandwidth B given by $P = kTB$, where k is Boltzmann's constant. Fig. 2 shows the setup of a radiometer placed on layer 1 (skin), with subsurface tissue layers (e.g., fat, muscle, etc.) denoted by layer 2, layer 3 etc. The radiometer receives radiation through the probe which is at a physical temperature T_p . The total power received from the tissue stack corresponds to a probe temperature $T = P/kB$. The tissues radiate power in the microwave frequency range proportionally to their conductivity. The tissue layer contributions are weighted also by the near-field radiation pattern of the probe and can be expressed as

$$T_A = \sum_{i=1}^N W_i(f, d_1, \sigma_1, \dots, d_i, \sigma_i, \dots, d_N, \sigma_N) T_i \quad (1)$$

where T_i is the physical temperature of the i th layer and W_i is the i th layer weighting function, which depends on frequency f , thickness d , and conductivity σ of all layers.

The blackbody curve peaks in the infrared range for a human body (310 K), but the penetration depth of skin at IR

TABLE I
DIELECTRIC PROPERTIES OF HUMAN TISSUES AND
SOME TISSUE PHANTOMS AT 1.4 GHz [35], [36]

Tissue	$\sigma(S/m)$	Permittivity	$\delta_S(cm)$
Skin	1.035	39.66	1.322
Fat (Infiltrated)	0.150	11.20	3.473
Fat (Non infiltrated)	0.064	5.395	5.317
Muscle	1.142	54.11	1.259
Salmon	1.510	52.50	1.095
Rogers 6010	0.002	10.20	30.08
Rohacell	2.45×10^{-5}	1.050	271.8
Saline (Salinity=9ppt, T=23°C)	1.570	78.00	1.074

is only 2 mm. At lower microwave frequencies, e.g., 1 GHz, the penetration depth of a plane wave is 3.2 cm for standard electrical parameters and tissue thicknesses. Table I gives values for average tissue properties and associated classical skin depth. It was shown in [37] that the penetration depth for a stacked tissue layer in the near field differs from the values in Table I. Therefore, plane-wave skin depth is not appropriate in this case, and the interaction of the probe with the tissue stack needs to be modeled in the near field. The fluctuation-dissipation theorem can be used to calculate the magnitude of a thermally fluctuating current density [23], but this method is not easily extended to arbitrarily shaped probes placed directly on the skin. Absorbed power is by reciprocity equivalent to radiated power, so determining the specific absorption rate through full-wave simulations, in this approach is used to infer the weighting functions described in (1) can be used to find the absorbed power in each layer.

Multifrequency radiometry can also be applied [10]–[12], [20], [21], [38], requiring multiple radiometers, thus increasing complexity, size, and cost. In this method, the estimated temperature is sensitive to the many unknown parameters, as discussed in [20]. Modeling the temperature profile with a bioheat transfer equation [39] adds a temperature estimate that improves the accuracy and stability of the retrieved spatial temperature profile [30], but information on heat rate, heat exchange, blood perfusion, and heat generation is difficult to predict. The goal of the research in this paper is not imaging—rather than being interested in the spatial temperature profile, the important quantity for the applications listed in Section I is tracking of internal temperature. Therefore, the temperature of intermediate layers is not of interest, and the mean temperature of the desired subsurface layer can be found with a single-frequency measurement. Unlike in imaging applications, our probe is not designed to have a small, well-defined focal point. Instead, it optimizes reception from the internal layer of interest (muscle in this case), while averaging over a lateral area of a few centimeters. This makes placement on the body less critical, and improves the accuracy of core temperature measurement.

An additional problem in temperature retrieval is low SNR. To measure internal tissue temperature at centimeter-depth under the skin, lower microwave frequencies are used, forcing operation on the tail of the blackbody curve. From this extremely low-power measurement, the temperature of a particular tissue layer needs to be retrieved. Note that the

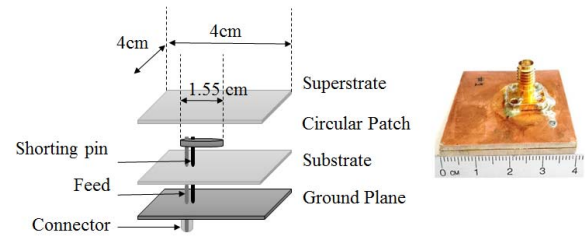


Fig. 3. Circular patch probe with superstrate and inductive shorting pin and photograph of the probe with a 4 cm \times 4 cm ground plane. The substrate and superstrate are Rogers 6010 material with $\epsilon_r = 10.2$ and 1.27 mm thick.

second mechanism of heat transfer, conduction, is characterized by a much longer time constant related to tissue thermal conductivity and capacitance, while the radiative transfer is practically instantaneous.

III. THERMOMETER DESCRIPTION

The frequency band of 1.4–1.427 GHz, allocated for radio astronomy, is selected as it provides a reasonable compromise between sensing depth, probe size, and background RFI. At higher microwave frequencies, the penetration depth reduces to a few millimeters, while at frequencies below 1 GHz, the spatial resolution associated with finite probe size is reduced [38]. The goal of this paper is long-term temperature monitoring and, therefore, the architecture is chosen toward implementing a wearable device [33]. In Fig. 1, the main parts of the system are the near-field probe, radiometer, and temperature-retrieval algorithm.

A. Probe Design

The skin-mounted probe needs to be small and conformal, and receives most of the power from the tissue stack with as little as possible from outside the body. Although the probe acts as a receiving antenna, standard antenna design and analysis is not directly applicable, since it is in the near field of the tissues.

A circular microstrip patch (Fig. 3) is chosen for its size and simplicity, as well as partial RFI shielding by the ground plane. The narrow bandwidth and inherent filtering of a patch is also beneficial for RFI mitigation since there are a number of cellular bands in the neighborhood of the quiet 1.4-GHz band. Although a wide measurement bandwidth is often desired in radiometry to achieve high temperature resolution, a narrow bandwidth may be compensated with integration time, as shown in (2). Core body temperature changes in the order of minutes and integration time less than 1 s is sufficient for this application. Since the thickness of tissue layers varies on different parts of the body, as well as from person to person, a superstrate is included to reduce the sensitivity of the probe to the surrounding media. A high-permittivity dielectric material, Rogers6010, and an inductive shorting pin to ground are used to reduce the overall size of the probe. The probe with a 4 cm \times 4 cm ground plane is shown in Fig. 3. For a more compact wearable probe, the size of the ground plane can be reduced by a factor of 4 (2 cm \times 2 cm) with only slight simulated increase in RFI reception.

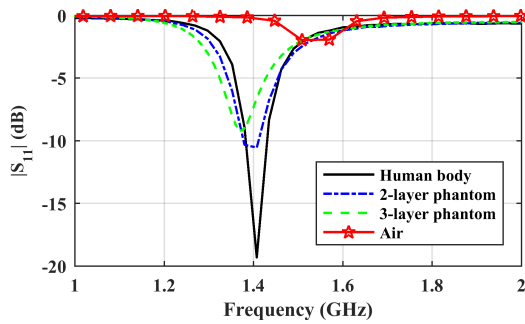


Fig. 4. Measured return loss of the probe when placed on the human body (cheek) showing the design is not optimized for an antenna in air. The probe is also measured on two different phantoms: a two-layer salmon-water stack and a three-layer stack of salmon, Rohacell foam and water.

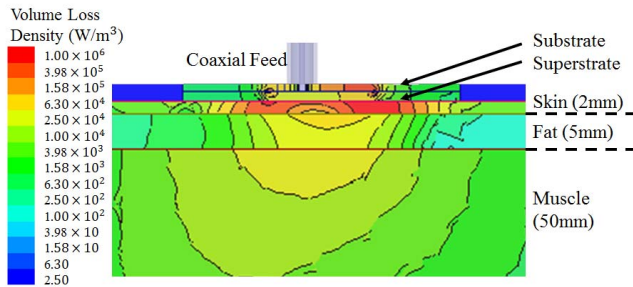


Fig. 5. Simulated volume loss density in W/m^3 of the proposed probe placed on the skin-fat-muscle stack, with a 1-W excitation at the matched feed point. The simulated stack has lateral dimensions of $12\text{ cm} \times 12\text{ cm}$.

Fig. 4 shows the measured return loss of the probe for several scenarios, including a real human body (cheek) and different tissue phantoms. The match at 1.4 GHz is better than 9 dB for all cases, with poor matching at the crowded cellular frequencies (0.9, 1.8, and 2 GHz). Although matching does not preferentially enhance the thermal noise power reception from the core tissue layers, it is important because it increases total power reception, helping to overcome the very low SNR.

The probe is designed to be matched to the human cheek model [40] and is optimized with HFSS using tissue properties listed in Table I. This procedure can be repeated for a probe that operates on a different part of the body. Although anatomical tissue layers change significantly throughout the body, the first layer (skin) has the biggest effect on the design of the probe, thus only tuning and optimization is required for other placements on the body. The radiated power received from a particular layer will by reciprocity be the same as the power absorbed by the same layer, which is quantified by volume power loss density, in W/m^3 . Fig. 5 shows simulated absorbed power in each tissue layer. Although fat has a low electromagnetic loss compared to skin and muscle, it absorbs a nonnegligible portion of the input power. This is due to the electric field boundary conditions and the predominantly normal electric field produced in the skin layer. Skin has a relative permittivity higher by an order of magnitude than that of fat, resulting in a higher electric field in fat.

Fig. 6 shows the simulated volume loss density under the center and edge of the patch probe from Fig. 3. A patch antenna radiates from fringing field at the edges, and therefore,

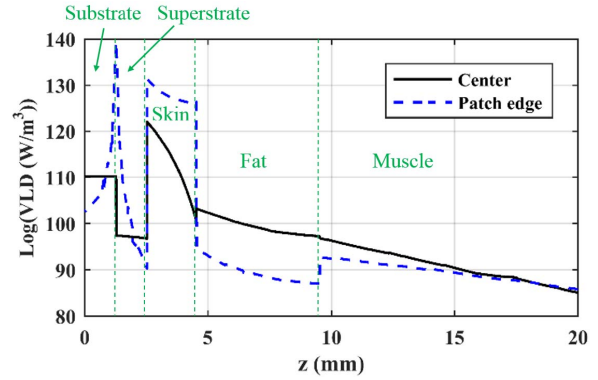


Fig. 6. Simulated volume loss density profile of the probe placed on the stack of skin, fat, and muscle. The z -axis is perpendicular to the skin surface with $z = 0$ at the ground plane of the conformal probe. The solid line corresponds to the center of the patch, while the profile below the patch edge is shown by dashed lines.

it is reasonable to expect that the volume loss density will be high at the probe edges between the substrate and superstrate. This trend is followed in the first tissue layer under the probe. However, due to boundary conditions, the fields from the edges of the patch add by superposition in the region under the probe, enhancing the loss density in the fat and muscle layers.

B. Radiometer Design

In order to detect very small temperature variations in deep tissue layers, the radiometer should have high sensitivity, low noise, low gain drift, and it should be stable. In this paper, a Dicke radiometer is designed from off-the-shelf surface-mount components, including a switch, two low-noise amplifiers (LNA), two bandpass filters, and a sensitive diode detector, detailed in Fig. 7. The size of the board is $8.2\text{ cm} \times 5\text{ cm}$, as illustrated in Fig. 7.

Considering 27 MHz of bandwidth for the quiet radio astronomy band and typical body temperature ($T = 310\text{ K}$), the probe should be receiving -100 dBm . In order to keep the input power well within the square-law region of the diode detector, approximately 45 dB of gain is required [32]. The radiometer components, listed in Table II, are selected to achieve this gain, with minimum cascaded noise figure.

The measured output voltage versus input power (voltage responsivity) and frequency response are shown in Fig. 8. The output voltage of the radiometer, in the square-law region of the output detector, is linearly related to the noise temperature of the input source. Therefore, it is sufficient to measure the output voltage corresponding to each of the two input noise temperatures to establish the calibration line, for converting the output voltage of the radiometer to probe radiometric temperature.

The precision with which temperature can be measured is often referred to as the radiometer sensitivity or radiometric resolution (ΔT), which is inversely proportional to integration time and system bandwidth [34]

$$\Delta T = \frac{T + T'_{\text{rec}}}{\sqrt{B\tau}} \quad (2)$$

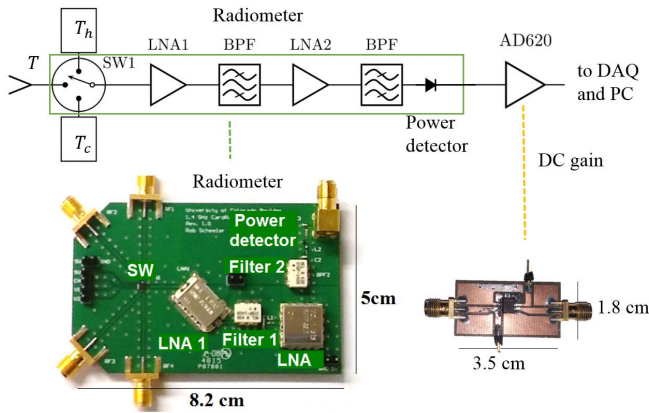


Fig. 7. Block diagram of radiometer showing hardware prototypes built from off-the-shelf components.

TABLE II
COMPONENTS OF THE 1.4-GHz RADIOMETER

Component	G(dB)	NF(dB)	Part number	Manufacturer
SW ₁	-0.55	0.55	SKY13388-465LF	Skyworks
LNA ₁	35	0.6	Tamp-1521GLN+	Mini-Circuits
BPF _{1/2}	-4.14	4.14	SYBP-1420	Mini-Circuits
LNA ₂	18.5	1.1	Ramp-33LN+	Mini-Circuits

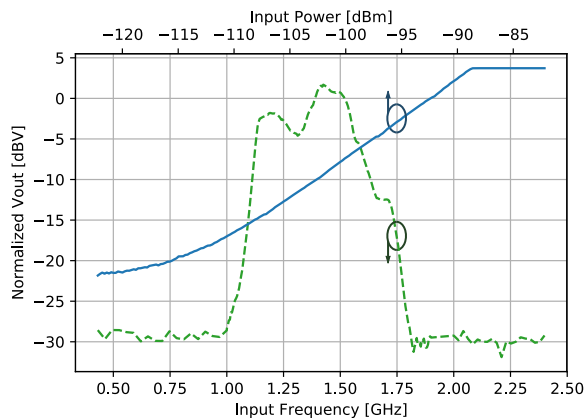


Fig. 8. Measured frequency response (bottom axis) at -92 dBm of input power and voltage responsivity of the radiometer at 1.4 GHz (top axis).

where T is the probe temperature, T'_{rec} is the radiometer noise temperature, B is the bandwidth, and τ is the integration time. For a resolution of $\Delta T = 0.2$ K and an integration time of $1/3$ s, the maximum radiometer noise temperature is 290 K.

The measured voltage frequency response, gain, and noise figure of the radiometer, using an HP 9870B noise figure meter, demonstrate a gain of 46.5 dB and a noise figure of 1.58 dB (Fig. 9). The frequency response is measured at 1.4 GHz at an input power of -92 dBm. Even though the radiometer cannot amplify the strong interference at 1.9 GHz, the bandwidth needs to be reduced to the 27 MHz of the quiet band to minimize interference. Although such a bandpass filter is not practically achievable with low loss and a small footprint suitable for wearable applications, the inherently narrow bandwidth of a patch radiator allows us to restrict reception to this quiet band.

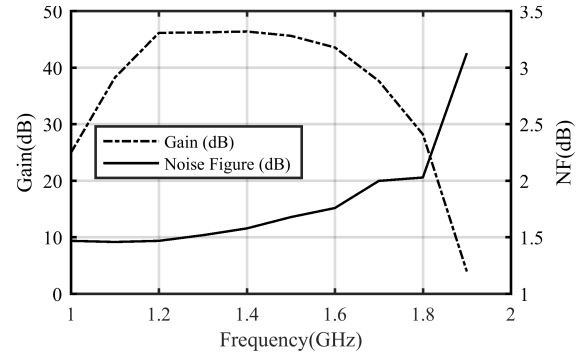


Fig. 9. Measured gain and noise figure of the radiometer over frequency.

IV. TEMPERATURE RETRIEVAL

In order to estimate the subsurface tissue layer temperature, the first step is to express the radiometric temperature of the probe at the feed point (T) in terms of the temperatures of all relevant tissue layers as given in (1). Referring to Fig. 2, for the case of three layers this becomes

$$T = \sum_{i=1}^3 W_i T_i = T_1 W_1 + T_2 W_2 + T_3 W_3 \quad (3)$$

where T_i is the temperature of the i th layer and W_i is the i th layer weighting function, which depends on frequency, thickness (d) of each layer, physical temperature, and conductivity of the materials as well as near-field probe pattern. The power dissipated in a particular layer normalized to the total dissipated power gives the following expression for the weight of each layer:

$$W_i = \frac{P_{\text{di}}(r)}{P_d} \quad (4)$$

where P_{di} is the power dissipated in the i th layer and P_d is the total dissipated power in the volume. The volume used for calculating the weights is bound by power loss density values below 10 W/m^3 , referring to Fig. 5. We feel this is a good approximation since a very small amount of power is absorbed by the remaining volume.

With these assumptions, the radiometer temperature is first corrected for the probe reflection coefficient

$$\begin{aligned} T' &= (1 - |\Gamma|^2)T + |\Gamma|^2 T_r \\ T_r &= \frac{1}{L} T'_{\text{rec}} + \left(1 - \frac{1}{L}\right) T_{\text{rm}} \end{aligned} \quad (5)$$

where Γ accounts for the impedance mismatch of the probe, and T_r is incident on the probe from the receiver and cable. The radiometer temperature is next corrected for the loss in the cable as

$$T'' = \frac{1}{L} T' + \left(1 - \frac{1}{L}\right) T_{\text{rm}} \quad (6)$$

where L is the loss factor, defined as $1/G$ for a less-than-unity gain. This procedure corrects the radiometric observations up to the plane of the radiometer (shown with dashed line

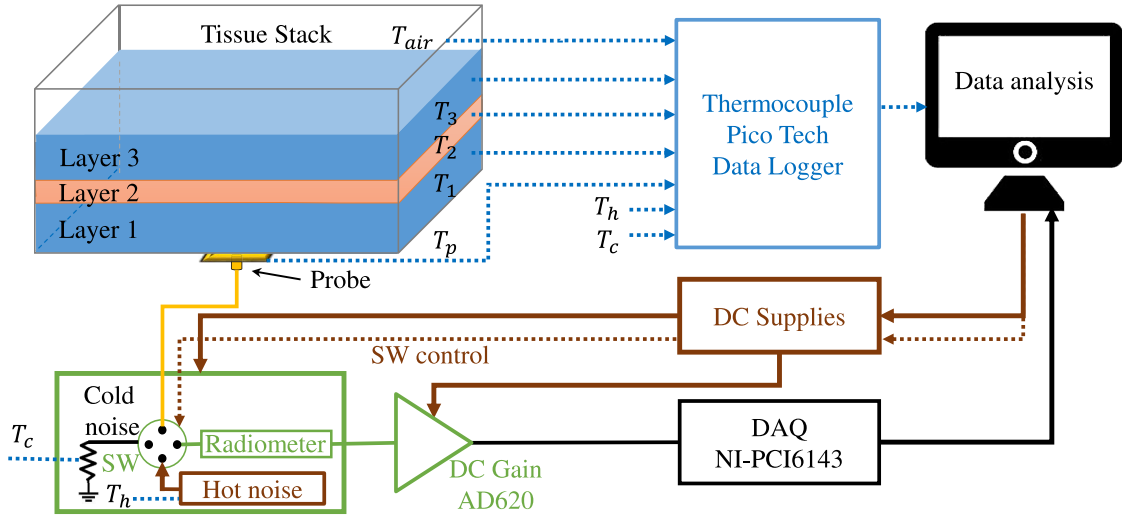


Fig. 10. Block diagram of measurement setup showing a stack of tissue layers placed on top of the probe. The probe feed is connected to the input port of a SP3T switch with the other two ports connected to the hot and cold noise sources. The output of the radiometer described in the previous section is amplified by a dc-gain block and digitized for processing. Four additional thermocouples are used for independent temperature measurement.

in Fig. 2). Given these adjustments, the radiometer output voltage when the probe is selected by the input switch is

$$V_{\text{probe}} = \mu [T'_{\text{rec}} + b_p T'' + (1 - b_p) T'_{\text{rec}}] \quad (7)$$

where $\mu = C_d G k B_{\text{rec}}$ represents the total receiver conversion factor from a temperature in K to an output value in V, for a detector sensitivity of C_d , a gain of G , and receiver bandwidth B_{rec} . The factor $b_p = B_{\text{probe}}/B_{\text{rec}}$ accounts for a probe with a narrower bandwidth than the receiver. Since the reference noise sources are matched across the receiver bandwidth, their measured voltage is simply

$$V_{\text{ref1,2}} = \mu [T'_{\text{rec}} + T_{\text{ref1,2}}]. \quad (8)$$

With these inputs measured sequentially over a 1-s ($\tau = 1$ s) period, the output voltage of the radiometer is

$$V_{\text{out}} = \begin{cases} \mu [T'_{\text{rec}} + b_p T'' + (1 - b_p) T'_{\text{rec}}], & 0 < t < \tau/3 \\ \mu [T'_{\text{rec}} + T_{\text{ref1}}], & \tau/3 < t < 2\tau/3 \\ \mu [T'_{\text{rec}} + T_{\text{ref2}}], & 2\tau/3 < t < \tau. \end{cases} \quad (9)$$

The use of two different reference sources at known physical temperatures T_{ref1} , T_{ref2} allows for real-time characterization of the receiver conversion factor μ and noise temperature T'_{rec}

$$\mu = \frac{V_{\text{ref2}} - V_{\text{ref1}}}{T_{\text{ref2}} - T_{\text{ref1}}} \quad T'_{\text{rec}} = T_{\text{ref1}} - \frac{V_{\text{ref1}}}{\mu}. \quad (10)$$

Solving (7) for T'' gives

$$T'' = \frac{V_{\text{probe}}}{\mu b_p} + \left(1 - \frac{2}{b_p}\right) T'_{\text{rec}} \quad (11)$$

where b_p is computed from separate bandwidth measurements of the probe and the receiver, as shown in Figs. 4 and 8. Inverting (6) and (5), we obtain the radiometric temperature sensed by the probe T

$$T' = LT'' + (1 - L)T_{\text{rm}} \\ T = \frac{T' - |\Gamma|^2 T_r}{1 - |\Gamma|^2}. \quad (12)$$

Finally, to extract the temperature of the core muscle layer, consider (3) where layer 2 (fat) temperature is the average of layer 1 (skin) and layer 3 (muscle)

$$T = T_1(W_1 + W_2/2) + T_3(W_3 + W_2/2). \quad (13)$$

Radiometric temperature T from (12), the direct measurement of surface temperature T_1 with a thermocouple, and the extraction of W_1 , W_2 , and W_3 from a full-wave simulation allow us to solve the desired internal temperature

$$T_3 = \frac{T - T_1(W_1 + W_2/2)}{W_3 + W_2/2}. \quad (14)$$

V. EXPERIMENTAL VALIDATION

Before *in vivo* tests, phantom measurements of multiple-layer tissues are performed in order to validate the approach in a controlled environment with a single-layer phantom, as well as two- and three-layer phantom tissue stacks, approximately 10 cm \times 10 cm, which is large enough that the edges do not interact measurably with the probe. An overall block diagram of the measurement setup is shown in Fig. 10. The probe is placed directly on the first layer and connected to the radiometer along with the external hot and cold noise sources. The output voltage is measured by an analog-to-digital converter, with an added dc gain stage that results in the best resolution from the National Instruments PCI-6143 16-bit, 250 kS/s/ch, simultaneous sampling multifunction data acquisition unit (DAQ). The estimate of temperature at the radiometer plane is first corrected for the probe reflection coefficient and the cable loss (typically 0.3 dB). Separate thermocouples monitor the temperature recorded by a Pico Technology tc-08 data logger. The computer controls the dc supply, which controls the noise sources and the switch which operates at a 0.333-s switching period, determined by the achievable resolution, ΔT .

TABLE III
WEIGHTING FUNCTIONS OF DIFFERENT LAYERS USED FOR ALL MEASUREMENTS. MUSCLES 1 AND 2 REFER TO TAP WATER AND SALINE, RESPECTIVELY. FATS 1 AND 2 REFER TO ROGERS6010 AND ROHACELL, RESPECTIVELY

Measurement	W_{Probe}	W_{Skin}	W_{Fat}	W_{Muscle}
Single layer	0.360	0.640	-	-
Two-layer, muscle 1	0.100	0.560	-	0.340
Two-layer, muscle 2	0.100	0.210	-	0.690
Three-layer, fat 1	0.101	0.633	0.025	0.241
Three-layer, fat 2	0.145	0.650	0.010	0.205

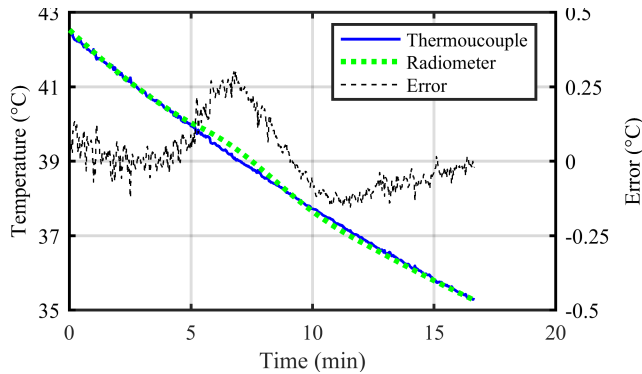


Fig. 11. Radiometric estimate of the temperature of a water half-space. The radiometer measurement is shown with a green dashed line, direct thermocouple measurement is shown in solid blue, and the error between the two is shown with a black dashed line. A low-pass filter is applied to the radiometer data.

A. Homogeneous (Single-Layer) Phantom Temperature Detection

The radiometer basic functionality is assessed with a single-layer 10-cm-deep water tissue phantom as shown in Fig. 10. The water is heated to about 43 °C and allowed to cool off over a period of 15 min. The estimate of the temperature at the radiometer plane is corrected for the probe reflection coefficient of -15 dB and a cable loss of 0.3 dB, as in (6). To estimate the actual temperature of the water, (3) is solved with weighting functions determined by HFSS and listed in Table III. The other half-space of the probe plane is assumed to be at room temperature. The radiometric temperature estimate is shown in Fig. 11 along with a thermocouple measurement of the water. The plot quantifies the error between the radiometric and independent thermocouple measurement, which is at most 0.4 °C.

B. Buried Layer Temperature Tracking

The previous experiment validated the operation of the probe and the radiometer and its ability to measure temperature with a subdegree accuracy. The real challenge, however, is to measure the temperature of a layer of tissue that is not directly in contact with the probe. For this validation, a 2-mm-thick layer of smoked salmon is used as a skin phantom [36] and water is used as a muscle phantom. Two cases are presented in order to validate the effect of electrical conductivity of a buried tissue layer. The experiment is described in Fig. 12.

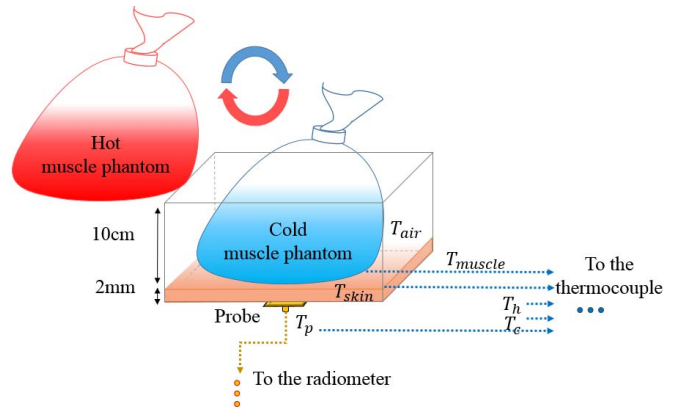


Fig. 12. Block diagram of two-layer measurement setup showing a probe connected to the radiometer measurement setup. Two plastic bags filled with 1.5 L of cold and hot muscle phantom are periodically cycled and placed on a 2-mm-thick skin phantom. The goal is measuring the temperature of unknown muscle phantom with the radiometer probe in direct contact with the skin. One thermocouple is placed on the skin and used in the temperature extraction algorithm, while the others are used for verification.

Measured temperature tracking is shown in Fig. 13(a) as a plastic bag filled with tap water is cycled between 10 °C and 79 °C, while Fig. 13(b) shows the same measurement but with a saline solution cycled between 15 °C and 30 °C. The inverse problem i solved using (2) for $i = 1, 2$ where the weighting functions are again obtained from full-wave simulations and are given in Table III. The temperature of first layer is measured using a thermocouple.

The main conclusions from the plots in Fig. 13 are: 1) the radiometer tracks the subsurface temperature and 2) the thermal conduction is characterized by a much longer time constant, in the order of tens of seconds, while the radiometric measurement is practically instantaneous since it occurs at the speed of light through tissue. Note that in Fig. 13(a), there is a slight temporal offset between the radiometer and thermocouple data, due to the fact that the thermocouple was not in direct contact with the water phantom for this specific case. Another interesting observation is that the estimated subsurface temperature is affected by the conductive heating of the salmon layer, which is seen from the slope of the estimated temperature for the time periods of hot and cold water. This is easily seen from the two-layer estimation expression

$$T_{\text{water}} = \frac{T - T_{\text{salmon}}W_{\text{salmon}} - T_{\text{probe}}W_{\text{probe}}}{W_{\text{water}}} \quad (15)$$

where when T_{salmon} slowly increases due to conduction, the estimated water temperature decreases.

C. Three-Layer Buried Layer Temperature Tracking

Increasing the number of layers to include a phantom layer of fat adds another term to the estimation (3). To demonstrate this more complex case, a 1.27-mm thick layer of Rogers 6010 Duroid substrate is added between the salmon and bag of saline, representing a layer of fat (see Table I). The experiments are performed as illustrated in Fig. 12 with an additional layer added, and the results are plotted in Fig. 14(a). The weighting functions for two fat phantoms are given

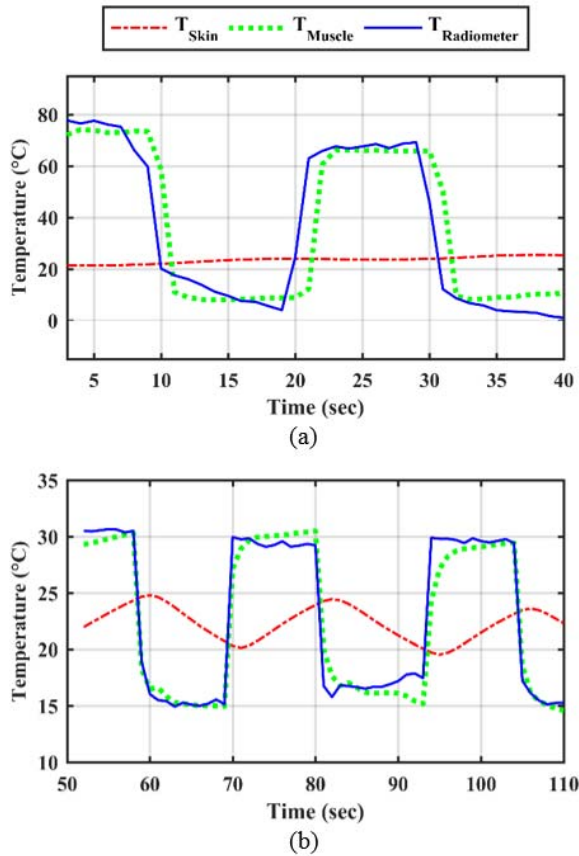


Fig. 13. Measured subsurface temperature tracking of a two-layer phantom with muscle represented by (a) tap water and (b) 9-ppt saline solution. In (a), the buried layer temperature is varied over a wide range from 10°C to 79°C, while in (b) the variation is smaller (10°C to 31°C). The red line shows the measured salmon (skin) temperature. The solid blue line shows the radiometric estimation of the muscle temperature, while the dashed green and red lines show data from thermocouples placed on the muscle and skin phantoms, respectively.

in Table III. Again, the radiometer has sufficient sensitivity to track the temperature of layer 3 under two other layers. To assess the long-term stability of the measurement, the Duroid layer is replaced by a 3-mm layer of Rohacel foam ($\epsilon_r = 1.05$), the tap water phantom is heated to 60 °C, and the temperature is measured as it cools to 45 °C over a 2.5-h time period at room temperature [Fig. 14(b)]. The discrepancy between the thermocouple and calibrated radiometric measurement increases after about 1.5 h, resulting in an error as large as 5 °C. This is attributed to RFI which increases the total power received from the probe, but does not strongly affect the power measured from the hot and cold noise sources, as would thermal drift of the receiver. Section V-D describes one way to mitigate RFI with a second probe.

D. Radio Frequency Interference Mitigation

The extremely low level of microwave power emitted by the human body can be masked by weak interference even when operating in the 1.4-GHz quiet band. Strong signals in neighboring bands, such as cellular communications at 1.8 and 1.9 GHz, cause unpredictable fluctuations (usually spikes) in the measurements. Interference may also come from

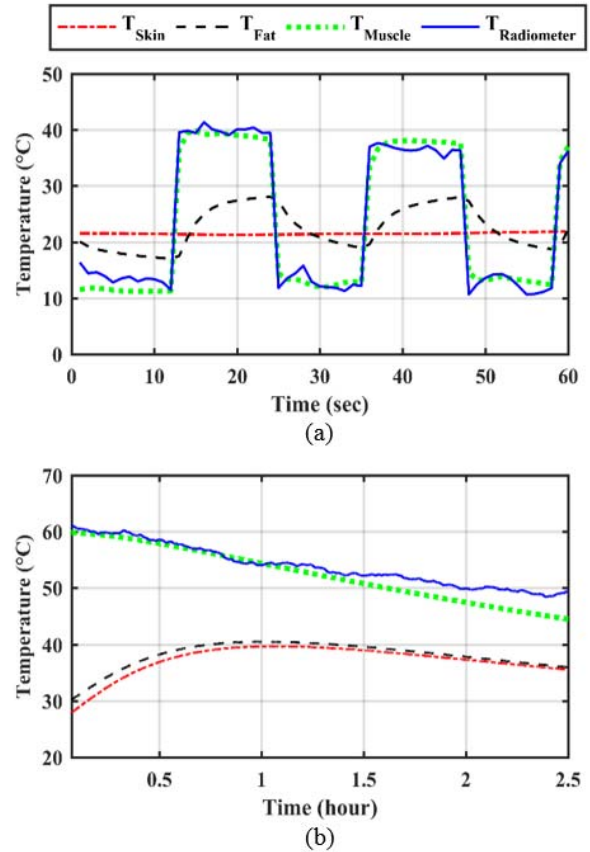


Fig. 14. Two buried temperature measurements over different time scales, where all thermocouple measurements are performed at the outer interface of the subscript layer, e.g., T_{fat} is measured at the interface between the fat and skin (phantom) layers. (a) Subsurface temperature tracking of the buried muscle (9-ppt saline) temperature under the stack of skin (2-mm salmon) and fat (1.27 mm of Rogers6010). (b) Radiometric estimate of the temperature of a muscle (tap water) layer under 3 mm of fat (Rohacel foam) and 2-mm layer of skin (smoked salmon) over a period of 2.5 h.

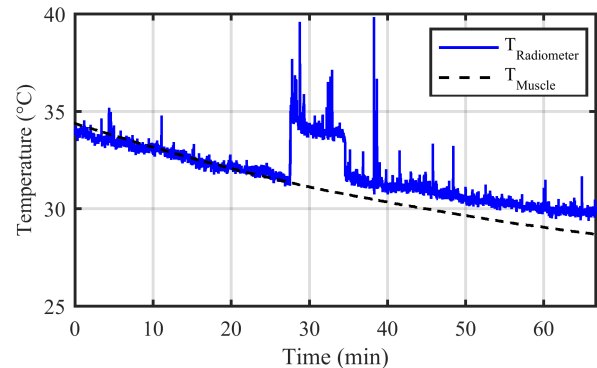


Fig. 15. Buried muscle (water phantom) under skin (salmon) and fat (Rohacel) measurements in the presence of RFI shows larger errors in temperature estimation when external signals are received by the probe.

household devices such as fluorescent lights. An example measurement for the three-layer phantom stack with RFI present is shown in Fig. 15. Although the measurements were done in a relatively radio-quiet basement, in this case, after 27 min some interference was observed.

To reduce the effect of interference, a direct measurement with a second probe is performed and an estimate of the

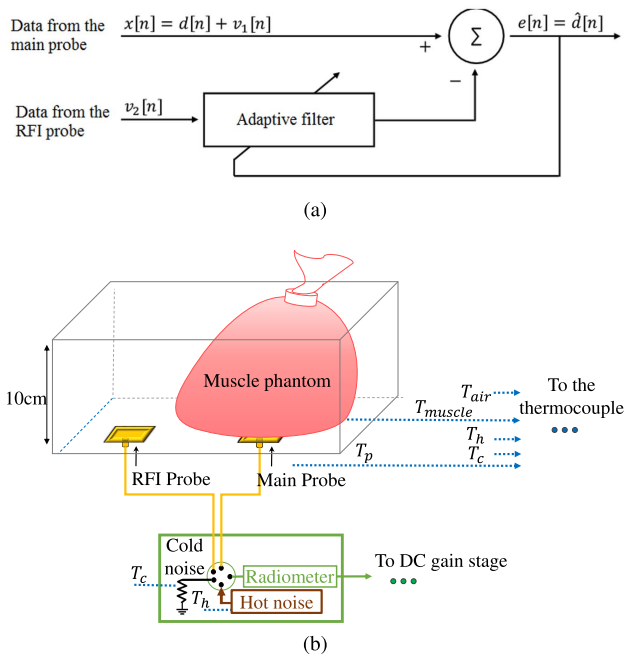


Fig. 16. (a) Signal diagram of adaptive interference cancellation algorithm. (b) RFI observation setup.

interference is subtracted from the main probe measurement. Although the main probe detects both RFI and noise power from the body, the RFI probe is situated such that it does not couple significantly to the body (or phantoms) and thus measures only RFI. For finite-sized phantoms, the RFI probe may be placed to the side, as shown in Fig. 16(b); however, for a human body, it would be placed facing away. Consider the total signal measured by the radiometer expressed as a discrete signal after sampling

$$x[n] = d[n] + v_1[n] \quad (16)$$

where $d[n]$ is the desired noise signal, $v_1[n]$ is RFI, and $x[n]$ is the measured total signal. The relative power of the RFI is often greater than that of the blackbody radiation, but is attenuated through the tissues. Furthermore, information regarding the process underlying $v_1[n]$ is generally unknown, making it more difficult to separate the desired signal from the interference. To address this, an adaptive interference cancellation technique is applied. A reference signal $v_2[n]$ that is correlated with $v_1[n]$ is used to formulate an estimate $\hat{d}[n]$ [Fig. 16(a)]

$$\hat{d}[n] = x[n] - \hat{v}_2[n]. \quad (17)$$

An additional probe is used to observe the environmental RFI [Fig. 16(b)] resulting in a measured signal $v_2[n]$ which tracks $v_1[n]$. The measurements are done sequentially, resulting in calibratable time misalignment. We assume that neither $v_2[n]$ nor $v_1[n]$ are correlated with $d[n]$. $v_2[n]$ is adaptively filtered in order to produce an estimate $\hat{v}_2[n]$, and a recursive least squares algorithm is used to generate the filter coefficients. The goal of this algorithm is to minimize the

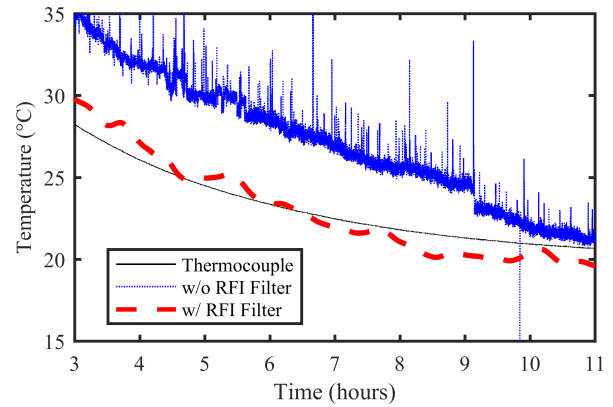


Fig. 17. Single-layer temperature estimation using the setup from Fig. 16(b) with an additional probe and adaptive algorithm, compared with an uncorrected measurement. The direct thermocouple measurement is also shown as a baseline.

weighted least squares error

$$\epsilon = \sum_{i=1}^n \beta(n, i) |e(i)|^2 \quad (18)$$

where $e(i)$ is the difference between the measured signal $d[n]$ and the estimated interference $\hat{v}_2[n]$. The weighting factor $\beta(n, i)$ is used to ensure that past data are forgotten in order to compensate for the nonstationary RFI nature. Therefore, the adaptive filter can follow the statistical variations of the observed data and extract an approximately interference-free estimate of the radiometer signal. Fig. 17 shows the resulting temperature estimate in comparison with the uncorrected measurement.

VI. DISCUSSION AND CONCLUSION

The experiments in the previous section demonstrated the feasibility of noninvasive temperature measurements of buried tissue layers using controllable tissue phantoms. There are a number of applications where internal body temperature measurements are critical. Examples include brain temperature monitoring of infants suffering from hypoxia-ischemia, measuring heating due to inflammations such as arthritis, cancer detection, urine flow monitoring, hyperthermia temperature control, and monitoring drug delivery. Some of the applications can be performed clinically, while others benefit from long-term monitoring. Since the tissue stacks differ, the probe should be redesigned in each case, and available full-body tissue models (e.g., IT'IS virtual population [41]).

One example that requires only relative temperature tracking is monitoring the heart temperature of people under heavy training and emergency personnel. Another application that requires relative temperature is tracking the difference between the external temperature of the extremities and core temperature, related to changes in the circadian cycle which has been shown to be related to sleeping disorders, diabetes, and certain cancers. Such long-term monitoring requires wearable solutions which can store or transmit data. A wearable uncalibrated wireless radiometer, described in [42], is used to measure varied water temperature in a human mouth by placing the

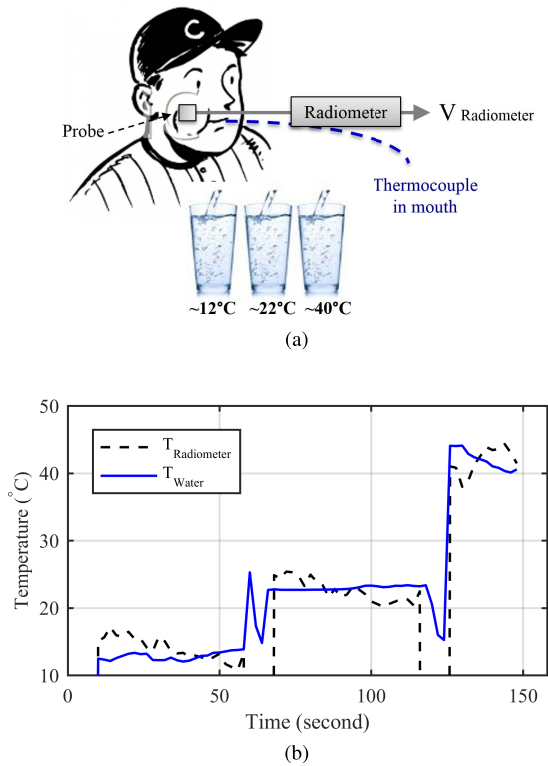


Fig. 18. (a) To change the temperature under the skin and tissue in the cheek, water at different temperatures fills the mouth. The goal is tracking water temperature with a probe on the skin. A thermocouple in the mouth directly measures the temperature of the water. (b) Calibrated radiometric temperature of the water inside the mouth, measured through the cheek and compared to a thermocouple measurement inside the mouth.

radiometer probe on the cheek. Similar measurements are performed with the calibrated Dicke radiometer as described in this paper, and using the circular patch with shorting pin and superstrate probe. Fig. 18(a) shows the probe positioned on the cheek. The probe is designed for the average thickness of cheek tissue layers (1.8-mm-thick skin layer, 4-mm-thick fat layer, and 2-mm-thick muscle layer). In order to change the temperature inside the oral cavity, cold, room temperature, and warm water is held in the mouth (Fig. 18). Radiometric readings observed over a time span of 200 s show that the radiometer tracks *in situ* temperatures measured by a thermocouple.

In addition to radiometer calibration which is continuously done with hot and cold noise sources switching, model calibration will also be required for practical applications, since tissue layers differ between individuals and body parts. In particular, the thickness of the fat layer exhibits a large variation. The sensitivity of the estimated temperature for different fat thicknesses is studied for the skin–fat–muscle model by varying the fat layer thickness from 2 to 8 mm. Weighting functions are calculated for each tissue stack and then used to estimate the input power to the radiometer using the same probe. The error in final estimated temperature is then calculated relative to an assumed fat thickness of 4 mm and is plotted in Fig. 19. The results show that the temperature error is less than 0.6 °C across a 4 °C range for a fat layer twice (8 mm) or half (2 mm) of the assumed thickness (4 mm).

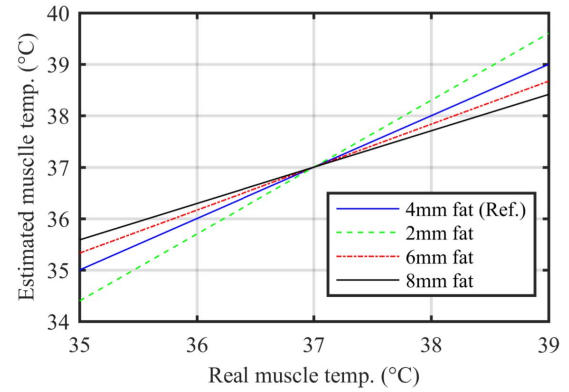


Fig. 19. Sensitivity of radiometric temperature to uncertainty in fat thickness. Radiometer outputs are simulated with weighting functions for different fat thicknesses, but all temperatures are retrieved assuming a thickness of 4 mm. Offsets are applied, simulating an independent temperature measurement of 37 °C at rest.

This in turn means that exact knowledge of the fat layer thickness is not required, especially in light of the fact that muscle temperature is not likely to vary more than 4 °C, even under extreme conditions.

In summary, this paper presents a study of near-field radiometry for internal temperature measurements of the human body using a portable Dicke radiometer in the 1.4-GHz quiet band. The total blackbody power from a tissue stack is received by a probe placed on the skin, designed to receive a high percentage of the total power from a buried tissue layer several centimeters in thickness. Temperature retrieval for subsurface tissue layers is performed using near-field weighting functions obtained from full-wave simulations. The calibrated radiometer is demonstrated to track the temperature of a phantom muscle tissue layer under phantom fat and skin layers within a fraction of a degree. *In situ* measurements on the human cheek show a good agreement with independent thermocouple measurements inside the mouth. It is shown that RFI can be reduced through the use of a second probe and adaptive processing. Simulations also show that the microwave thermometer is tolerant to fat layer thickness variation. The results from this paper show that a miniaturized, wearable, and more integrated microwave thermometer is feasible.

ACKNOWLEDGMENT

The authors would like to thank J. Wallingford of gaugewear, Inc. and Dr. J. Libove of Furaxa, Inc., for many useful discussions.

REFERENCES

- [1] Y. Eshraghi *et al.*, “An evaluation of a zero-heat-flux cutaneous thermometer in cardiac surgical patients,” *Anesthesia Analgesia*, vol. 119, no. 3, pp. 543–549, Sep. 2014.
- [2] K. Kräuchi, C. Cajochen, E. Werth, and A. Wirz-Justice, “Functional link between distal vasodilation and sleep-onset latency?” *Amer. J. Physiol.-Reg., Integr. Comparative Physiol.*, vol. 278, no. 3, pp. R741–R748, 2000.
- [3] N. E. Rosenthal *et al.*, “Effects of light treatment on core body temperature in seasonal affective disorder,” *Biol. Psychiatry*, vol. 27, no. 1, pp. 39–50, Jan. 1990.
- [4] J. E. Gale, H. I. Cox, J. Qian, G. D. Block, C. S. Colwell, and A. V. Matveyenko, “Disruption of circadian rhythms accelerates development of diabetes through pancreatic beta-cell loss and dysfunction,” *J. Biol. Rhythms*, vol. 26, no. 5, pp. 423–433, 2011.

- [5] D. Jeyaraj *et al.*, "Circadian rhythms govern cardiac repolarization and arrhythmogenesis," *Nature*, vol. 483, no. 7387, pp. 96–99, 2012.
- [6] Z. Popovic, P. Momenroodaki, and R. Scheeler, "Toward wearable wireless thermometers for internal body temperature measurements," *IEEE Commun. Mag.*, vol. 52, no. 10, pp. 118–125, Oct. 2014.
- [7] A. S. Howe and B. P. Boden, "Heat-related illness in athletes," *Amer. J. Sports Med.*, vol. 35, no. 8, pp. 1384–1395, 2007.
- [8] K. L. Carr, "Microwave radiometry: Its importance to the detection of cancer," *IEEE Trans. Microw. Theory Techn.*, vol. 37, no. 12, pp. 1862–1869, Dec. 1989.
- [9] J. Shaeffer, A. M. El-Mahdi, A. E. Hamwey, and K. L. Carr, "Detection of extravasation of antineoplastic drugs by microwave radiometry," *Cancer Lett.*, vol. 31, no. 3, pp. 285–291, Jun. 1986.
- [10] S. Jacobsen and P. R. Stauffer, "Multifrequency radiometric determination of temperature profiles in a lossy homogeneous phantom using a dual-mode antenna with integral water bolus," *IEEE Trans. Microw. Theory Techn.*, vol. 50, no. 7, pp. 1737–1746, Jul. 2002.
- [11] S. Mizushima, M. Matsuda, K. Matsui, Y. Hamamura, and T. Sugiura, "Non-invasive temperature profiling using multi-frequency microwave radiometry in the presence of water-filled bolus," *IEICE Trans. Electron.*, vol. 74, no. 5, pp. 1293–1302, May 1991.
- [12] J. W. Hand *et al.*, "Monitoring of deep brain temperature in infants using multi-frequency microwave radiometry and thermal modelling," *Phys. Med. Biol.*, vol. 46, no. 7, pp. 1885–1903, 2001.
- [13] D. S. Moran and L. Mendal, "Core temperature measurement," *Sports Med.*, vol. 32, no. 14, pp. 879–885, 2002. [Online]. Available: <https://www.ncbi.nlm.nih.gov/pubmed/12427049>
- [14] C. Byrne and C. L. Lim, "The ingestible telemetric body core temperature sensor: A review of validity and exercise applications," *Brit. J. Sports Med.*, vol. 41, no. 3, pp. 126–133, 2007.
- [15] D. M. Wilkinson, J. M. Carter, V. L. Richmond, S. D. Blacker, and M. P. Rayson, "The effect of cool water ingestion on gastrointestinal pill temperature," *Med. Sci. Sports Exercise*, vol. 40, no. 3, pp. 523–528, Mar. 2008.
- [16] G. Galiana, R. T. Branca, E. R. Jenista, and W. S. Warren, "Accurate temperature imaging based on intermolecular coherences in magnetic resonance," *Science*, vol. 322, no. 5900, pp. 421–424, Oct. 2008.
- [17] A. Guyton and J. Hall, *Textbook Medical Physiology*. London, U.K.: Artech House, 2000, pp. 159–178 and 251–257.
- [18] *What Your Life Looks Like In Thermal*. Accessed: Nov. 3, 2016. [Online]. Available: <https://youtu.be/48bwQVa0AQc?t=71>
- [19] L. Vanggaard, P.-E. Paulev, and G. Zubieta-Calleja, "Chapter 21: Thermo-regulation, temperature and radiation," in *New Human Physiology*, 2nd ed. Accessed: May 23, 2017. [Online]. Available: <http://www.zuniv.net/physiology/book/chapter21.html>
- [20] K. Maruyama *et al.*, "Feasibility of noninvasive measurement of deep brain temperature in newborn infants by multifrequency microwave radiometry," *IEEE Trans. Microw. Theory Techn.*, vol. 48, no. 11, pp. 2141–2147, Nov. 2000.
- [21] F. Bardati, V. J. Brown, and P. Tognolatti, "Temperature reconstructions in a dielectric cylinder by multi-frequency microwave radiometry," *J. Electromagn. Waves Appl.*, vol. 7, no. 11, pp. 1549–1571, 1993.
- [22] *Microwave Radiometry in Mammology*. Accessed: May 23, 2017. [Online]. Available: <http://resltd.ru/eng/radiometry/mom.php>
- [23] I. S. Karanasiou, N. K. Uzunoglu, and C. C. Papageorgiou, "Towards functional noninvasive imaging of excitable tissues inside the human body using focused microwave radiometry," *IEEE Trans. Microw. Theory Techn.*, vol. 52, no. 8, pp. 1898–1908, Aug. 2004.
- [24] K. D. Stephan, J. B. Mead, D. M. Pozar, L. Wang, and J. A. Pearce, "A near field focused microstrip array for a radiometric temperature sensor," *IEEE Trans. Antennas Propag.*, vol. 55, no. 4, pp. 1199–1203, Apr. 2007.
- [25] C. T. Huynh, R. Devine, and M. R. Tofighi, "An I-band microwave radiometer for subsurface temperature measurement," in *Proc. IEEE 16th Int. Symp. Consum. Electron. (ISCE)*, Jun. 2012, pp. 1–2.
- [26] M.-R. Tofighi and C. T. Huynh, "A microwave system for blood perfusion measurements of tissue; a preliminary study," in *Proc. IEEE Top. Conf. Biomed. Wireless Technol., Netw., Sens. Syst. (BioWireless)*, Jan. 2013, pp. 49–51.
- [27] M.-R. Tofighi, J. R. Pardeshi, and B. A. Maicke, "Microwave system and methods for combined heating and radiometric sensing for blood perfusion measurement of tissue," in *IEEE MTT-S Int. Microw. Symp. Dig.*, May 2016, pp. 1–4.
- [28] Q. Bonds, "A microwave radiometer for close proximity core body temperature monitoring: Design, development, and experimentation," Ph.D. dissertation, Dept. Elect. Eng., Univ. South Florida, Tampa, FL, USA, 2010.
- [29] O. Klemetsen, Y. Birkelund, S. K. Jacobsen, P. F. Maccarini, and P. R. Stauffer, "Design of medical radiometer front-end for improved performance," *Prog. Electromagn. Res. B*, vol. 27, pp. 289–306, 2011. [Online]. Available: <http://www.jpier.org/PIERB/pier.php?paper=10101204>, doi: 10.2528/PIERB10101204.
- [30] P. R. Stauffer *et al.*, "Stable microwave radiometry system for long term monitoring of deep tissue temperature," *Proc. SPIE*, vol. 8584, Feb. 2013, doi: 10.1117/12.2003976.
- [31] D. B. Rodrigues *et al.*, "Design and optimization of an ultra wideband and compact microwave antenna for radiometric monitoring of brain temperature," *IEEE Trans. Biomed. Eng.*, vol. 61, no. 7, pp. 2154–2160, Jul. 2014.
- [32] P. Momenroodaki, Z. Popovic, and R. Scheeler, "A 1.4-GHz radiometer for internal body temperature measurements," in *Proc. Eur. Microw. Conf. (EuMC)*, 2015, pp. 694–697.
- [33] P. Momenroodaki, W. Haines, and Z. Popovic, "Non-invasive microwave thermometry of multilayer human tissues," in *IEEE MTT-S Int. Microw. Symp. Dig.*, Jun. 2017, pp. 1387–1390.
- [34] F. T. Ulaby, R. K. Moore, and A. K. Fung, *Microwave Remote Sensing: Active and Passive. Microwave Remote Sensing Fundamentals and Radiometry*, vol. 1. Norwood, MA, USA: Artech House, 1981.
- [35] *Dielectric Properties of Body Tissues*. Accessed: Jun. 13, 2017. [Online]. Available: <http://niremf.ifac.cnr.it/tissprop/>
- [36] Y. Wang, J. Tang, B. Rasco, F. Kong, and S. Wang, "Dielectric properties of salmon fillets as a function of temperature and composition," *J. Food Eng.*, vol. 87, pp. 236–246, Dec. 2007.
- [37] R. Scheeler, E. F. Kuester, and Z. Popovic, "Sensing depth of microwave radiation for internal body temperature measurement," *IEEE Trans. Antennas Propag.*, vol. 62, no. 3, pp. 1293–1303, Mar. 2014.
- [38] H. Ohba, M. Kinomura, M. Ito, T. Sugiura, and S. Mizushima, "Multifrequency microwave radiometry for non-invasive thermometry using a new temperature profile model function," *IEICE Trans. Electron.*, vol. E78-C, no. 8, pp. 1071–1081, Aug. 1995.
- [39] E. H. Wissler, "A mathematical model of the human thermal system," *Bull. Math. Biophys.*, vol. 26, no. 2, pp. 147–166, 1964.
- [40] Ø. Klemetsen, S. Jacobsen, and Y. Birkelund, "Radiometric temperature reading of a hot ellipsoidal object inside the oral cavity by a shielded microwave antenna put flush to the cheek," *Phys. Med. Biol.*, vol. 57, no. 9, pp. 2633–2652, May 2012.
- [41] M.-C. Gosselin *et al.*, "Development of a new generation of high-resolution anatomical models for medical device evaluation: The virtual population 3.0," *Phys. Med. Biol.*, vol. 59, no. 18, p. 5287, 2014.
- [42] W. Haines, P. Momenroodaki, E. Berry, M. Fromandi, and Z. Popovic, "Wireless system for continuous monitoring of core body temperature," in *IEEE MTT-S Int. Microw. Symp. Dig.*, Jun. 2017, pp. 541–543.

Parisa Momenroodaki (S'07–GS'14), photograph and biography not available at the time of publication.

William Haines (S'15–GS'15), photograph and biography not available at the time of publication.

Michael Fromandi (S'14), photograph and biography not available at the time of publication.

Zoya Popovic (S'86–M'90–SM'99–F'02), photograph and biography not available at the time of publication.